LATERAL AERODYNAMICS CHARACTERISTICS OF FOREBODIES AT HIGH ANGLE OF ATTACK IN SUBSONIC AND TRANSONIC FLOWS

S. Koren[1], R. Arieli[2] and J. Rom[3]

ABSTRACT

The investigation of the pressure distributions on three elongated forebodies of revolution with circular cross section and different bluntness ratios are presented. Measurements are conducted at Mach numbers from 0.5 to 1.0 with angles of attack up to 45°. Some visualization data is obtained at transonic speeds by Schlieren-shadow photographs. The local lateral force along the axis at high angles of attack is calculated to emphasize the asymmetric flow regime that is developed. Effects of the variation of the angle of attack and Mach number are discussed.

1. INTRODUCTION

The continuing efforts to gain more understanding of the lateral aerodynamic characteristics of elongated configurations due to high angles of attack are directed towards the requirement of supermaneuverability of aircraft and missiles. Preliminary versions of next generation advanced fighters are being tested and flown presently at very exotic conditions of high incidence at low speeds. At low to moderate angles of attack a steady symmetrical flow pattern is established on the elongated forebody. This flow on the forebody is characterized by the separation of free shear layers which roll up into a symmetric pair of primary vortices, the increase of the angle of attack is accompanied by a pair of secondary vortices. At even higher angles of attack this symmetric vortex structure is transformed into a stable and steady asymmetric flow pattern. The asymmetric vortex structure generates a significant side force as well as large yawing moment on the elongated nose configuration.

The evaluation of the onset of asymmetry and improved description of the flow field is reported in many studies using mainly CFD methods [1],[2],[3]. Computed solutions of the Euler and Navier-Stokes equations demonstrate the abilities to correctly predict several important features of the complex three dimensional flow around a forebody at incidence. Some interesting solutions have been obtained even by using various panel methods [4],[5],[6]. However, all these numerical solutions must be tested against carefully controlled experimental data. The object of the present investigation is to provide pressure distribution data on sharp and blunt forebodies of revolution at low to high angles of attack and at subsonic to transonic speeds. This data complements the comprehensive measurements of forces and moments on similar models presented in ref. 7.

Details of the test facilities, the wind tunnel models and the instrumentation used in the present investigation as well as a description of the tests are presented in Chapter 2. The experimental results and a comparison with available data in order to demonstrate and verify the usefulness of the present data are discussed in Chapter 3. A discussion of the experimental results is presented in Chapter 4.

2. TEST FACILITIES

The current investigation is conducted in the transonic wind-tunnel at the Aeronautical Laboratory of the Israel Institute of Technology (IIT) in Haifa.

2.1 The transonic wind-tunnel

This transonic wind tunnel is an induction type tunnel[8] operated from a high-pressure compressed air supply. The test section of the wind tunnel is *60 cm x 80 cm*, and the Mach number range is $0.3<M<1.15$, with atmospheric stagnation pressure so that the Reynolds numbers per *cm* based on free stream conditions varies from 0.04×10^6 to 0.16×10^6 as the Mach number increases. In the settling chamber there is a honeycomb with hexagonal cell core of 3/8 *inches* and a length to width ratio of 11. It is followed by two fine turbulence suppression screens of 20 mesh and 30 mesh respectively. The nozzle contraction ratio is 16:1, followed by a rectangular *60 cm x 80 cm* test section with perforated ceiling and floor. The ceiling and the floor of the tunnel are diverging by an angle of 0.5° each, the side walls are parallel, vertical and solid. The *6 mm* diameter holes are in the top and bottom walls identical to the wall thickness and the solidity ratio of these perforated walls is 12%. The Mach number flow uniformity in the test section volume is within $\Delta M<\pm0.01$ over the transonic speed range.

[1]Graduate student, Department of Aerospace Engineering, IIT.

[2]Rafael, P.O.Box 2250, Haifa 31021, Israel.

[3]Lady Davis Chair, Department of Aerospace Engineering, IIT.

Copyright © 1992 by the American Institute of Aeronautics and Astronautics, Inc. and the International Council of the Aeronautical Sciences. All rights reserved.

2.2 Models and Instrumentation

Three different forebodies of revolution with a constant diameter and overall length of 8 calibers (fig. 1), are tested. The distribution of the pressure holes is matched to each one of the models to give suitable resolution at the junction between the nose and the afterbody, where large pressure variations are expected. At axial stations near the apex (section AA of fig. 1), pressure holes are positioned at $\Delta\phi=60^\circ$ apart, starting on the windward side at $\phi=0^\circ$ up to the leeward side at $\phi=180^\circ$, on the right hand side of the model pressure holes are located at 240° and 300°, an extra hole is added at $\phi=270^\circ$ in order to check the symmetry of the pressure on both sides of the body. On the left hand side, they are located at 30°, 90° and 150°. At more distant axial stations (e.g. section BB of fig. 1), pressure holes are distributed with intervals of $\Delta\phi=30^\circ$, on the right side of the model the holes are at $\phi=210^\circ$, 240°, 270°, 300°, and 330°. On the left hand side the pressure holes are positioned at $\phi=15^\circ$, 45°, 75°, 90°, 105°, 135° and 165°. At further downstream axial stations (e.g. section CC of fig. 1), the number of holes is diluted to 6 circumferential holes, at $\phi=0^\circ$, 45°, 90°, 180°, 225°, 270°. In the blunted forebodies, e.g. the hemisphere and the blunted tangent ogive, one hole is added at the apex. To sum up, the hemisphere model contains 83 pressure holes, the blunted tangent ogive model has 113 pressure holes and the von-Karman ogive model contains a total of 104 pressure holes. This distribution of pressure holes allows for a very good coverage of the surface pressure when the flow regime is symmetric, since the resolution of the measurements on each side can be doubled by using the mirror reflection to the other side. At high incidences, in order to get higher resolution, the model is rotated to roll angles of $\pm15^\circ$ and $\pm45^\circ$.

The pressure is measured by an electronically scanned pressure measuring system. This system uses multiple processors, equal in number to the number of the measurement points in order to attain high performance. The processors operate in a coordinated network that provides speed as well as synchronized control. The resolution of the system is of 16 bits and the accuracy is of $\pm0.05\%$ of the full scale. Unit processors also have 256 k-bits local memory for buffered retention of data. A diagram of the system is presented in fig. 2. The model is attached to a rigid sting and the angle of attack is measured by an accelerometer with an accuracy of $\pm0.01^\circ$. Some visualization data is obtained by Schlieren-Shadow photographs recorded on video tape and on film.

2.3 Wind-tunnel Tests

The pressure distribution on each model, is measured at several constant incidence and a constant Mach number. Tests are conducted at Mach numbers 0.5, 0.9 and 1.0 with angles of attach of 0°, 5°, 15° and 25°. Tests with $\alpha=45^\circ$ are conducted only at M=0.5 due to wind tunnel limitations. The model is rotated to roll angles of $\pm15^\circ$ and $\pm45^\circ$ to get a sufficient resolution of pressure measurement holes on each side of the model. In order to be consistent with the forces and moments experiments[7], the tests at M=0.9 are conducted at $\alpha=27^\circ$ and at M=1.0 at $\alpha=27.5^\circ$.

3. EXPERIMENTAL RESULTS

3.1 The hemisphere cylinder model

The pressure distribution on the surface of the hemisphere nosed model is presented as a function of the circumferential angle, at different axial stations. The pressure variation at several angles of attack and Mach numbers, are presented in figs. 3a to 3g. At M=0.5 and $\alpha=15^\circ$ (fig. 3a), the pressure coefficient at $x/D\leq0.35$ descends from the stagnation value at $\phi=0^\circ$ (the windward side) to a minimum at $\phi=180^\circ$ (the leeward side). Downstream, at x/D=0.50 a local maximum is measured on the leeward side of the model, forming two points of minimum pressure at $\phi=135^\circ$ and $\phi=225^\circ$ respectively. This behavior of the pressure distribution indicates a separated flow, probably from the nose separation bubble which reattaches and creates a local pressure peak. At further downstream axial stations the gradients become more shallow, but the basic variation is maintained. The local maximum at $\phi=180^\circ$, can be attributed to the reattachment of the cross flow, this flow separates at approximately $\phi=90^\circ$ and $\phi=270^\circ$. The flow is seen to be symmetric. Increasing the Mach number causes the appearance of a shock wave and a massive separation, seen in the Schliren photograph presented in fig. 4. The acceleration of the flow on the nose due to the increase of the free stream speed causes a premature separation and an increase of the pressure at x/D=0.35 on the leeward side (fig. 3b). The acceleration of the flow in the axial direction after the nose, contributes to the gradual disappearance of this maximum until the normal shock is met at approximately x/D=2.00. At this axial station and further downstream, the behavior is similar to the M=0.5 behavior at the same axial stations. With a further increase of the Mach number to M=1.0, a weak separated normal shock appears upstream of the body and the pressure recovery on the leeward side is increased (fig. 3c), but the basic behavior remains as at M=0.9. It should be noted that Hsieh[9] found out that at transonic speeds, above a critical Mach number, the nose separation bubble disappears and a well defined shock system replaces it. While in the present investigation the appearance of the normal shock is seen, the separation bubble seems to open up and become a massive separation region. At $\alpha=25^\circ$ and M=0.5 one can see that the pressure distributions observed at $\alpha=15^\circ$ remain basically unchanged, although the gradients in the circumferential direction become bigger (fig. 3d). The same qualitative agreement is seen when comparing the measurements at M=0.9 and $\alpha=27^\circ$ with those at M=0.9 and $\alpha=15^\circ$ (fig. 3e) and at M=1.0 and $\alpha=27.5^\circ$ with those at M=1.0 and $\alpha=15^\circ$ (fig. 3f). It is interesting to note that the flow is practically symmetric at M=0.5, $\alpha=25^\circ$ and at M=1.0, $\alpha=27.5^\circ$. At M=0.9, $\alpha=27^\circ$ a slight asymmetry is seen at $x/D\geq2.0$, the fact that the flow regime is found to be symmetric at M=0.5 and M=1.0 and slightly asymmetric at M=0.9, coincides well with the side

force measured on an hemisphere forebody in the same conditions (ref. 7). The asymmetrical flow regime is clearly seen at $\alpha=45^\circ$ and M=0.5 (fig. 3g). Since the asymmetry is expected, tests at several roll angles are conducted, in order to increase the resolution on both sides. The consistency of the measurements at different roll angles is presented in fig. 5, and is seen to be satisfactory, so that average values of the pressure measurements are used in fig. 6g. Near the nose of the model, the asymmetry is small and is concentrated near the leeside. At $x/D\geq0.8$ the asymmetry becomes noticeable in the zone of $90^\circ\leq\phi\leq270^\circ$, at $x/D\geq1.25$ a decrease of pressure at approximately $\phi=165^\circ$ and $\phi=195^\circ$ indicates the appearance of secondary vortices which induce higher velocities near the surface thus decreasing the local pressure coefficient. Further downstream the point of maximum pressure recovery moves from $\phi=180^\circ$ to $\phi\approx225^\circ$, pointing out that the vortices on both sides are of different strength, thus shifting the reattachment point of the cross-flow.

3.2 The von-Karman-ogive cylinder model

The surface pressure distribution on the von-Karman-ogive cylinder model, at different axial stations, for several angles of attack and Mach numbers, are presented in figs. 6a to 6g. At $\alpha=15^\circ$ and M=0.5 (fig. 6a), for all the axial stations that are tested, the pressure coefficient decreases from the cross-flow stagnation value at $\phi=0^\circ$, to minimum values at $\phi=90^\circ$ and $\phi=270^\circ$ and then increase to a local maximum at $\phi=180^\circ$. Although the pressure gradients are small, this structure indicates that there is a symmetric cross-flow separation on both sides and a reattachment at $\phi=180^\circ$, along the entire model. This observation is in good agreement with the oil film technique photographs presented in ref. 7 and with the data presented in ref. 12. Increasing the Mach number at the same angle of attack, does not affect the pressure distributions on the model (figs 6b, 6c). At $\alpha=25^\circ$ and M=0.5, the traces of what appears to be secondary vortices are observed (fig. 6d). At $x/D\geq4.0$ the secondary vortices are not detected any more. This "disappearance" is due to insufficient resolution of the pressure holes. As the Mach number is increased to M=0.9, the description of the pressure distributions becomes even clearer (fig. 6e). In contrary to what is seen with the hemisphere model, in this model no formation of a significant shock system is observed, due to the sharp nose and slenderness of the model. It is interesting to note that a slight asymmetry is observed at $x/D\geq5.0$. At M=1.0 the merging of the main and secondary vortices causes a shift of the minimum pressure points from $\phi\approx90^\circ$, 270° to $\phi\approx135^\circ$, 225° (fig. 6f), at x/D=4.0. Further downstream the minimum pressure points move apart again.

At $\alpha=45^\circ$ and M=0.5, the flow field is found to be asymmetric at all the axial stations tested (fig. 6g). In order to increase the resolution of the measurements, tests at several roll angles are conducted. In contrary to the results with the hemisphere model, the measured pressures at different roll angles are found to be dependent on the roll angle specially those measured near the nose of the model (figs. 7a, 7b), thus implying that the flow field on a sharp axisymmetric body is influenced by its roll angle. This is in agreement with the results of Degani et al[10]. who attribute the influence of the roll of the model to effects of the manufacturing imperfections in the vicinity of the apex on the formation of the separated vortices. It is interesting to note that the clear traces of secondary vortices seen at moderate angles of attack, are substituted here by a flat and wide maximum peak at $120^\circ\leq\phi\leq240^\circ$ and relatively wide minimum peaks at $75^\circ\leq\phi\leq105^\circ$ and $255^\circ\leq\phi\leq285^\circ$ respectively.

3.3 The blunted-ogive cylinder model

The surface pressure distributions as measured on the blunted ogive cylinder model, are presented in figs. 8a, 8f. These figures describe the variation of the pressure at different axial locations, as a function of angle of attack and Mach number. Fig. 8a presents the pressure distribution at M=0.5 and $\alpha=15^\circ$. At station x/D=0.1, at $\phi=180^\circ$ a minimum value of the pressure is obtained. It then flattens out while stepping downstream, to a plateau of constant pressure on the leeward side. At x/D=1.25 the formation of pressure peaks on the leeside of the model are evident, indicating the presence of cross flow separation and reattachment. As the Mach number is increased while maintaining the same angle of attack (figs. 8b, 8c), the recovery peak moves upstream, with no severe variations in the overall pressure field. This dependency of the pressure recovery peak and location, with Mach number, is probably due to the presence of the oblique shock seen in fig. 9 and the accompanied flow separation in the vicinity of the ogive-cylinder junction. At M=0.5 and $\alpha=25^\circ$, the formation of what appears to be a pair of secondary vortices is observed at $x/D\geq1.25$ and at circumferential position of $\phi=165^\circ$ and $\phi=195^\circ$ (fig. 8d). At $x/D\geq3.0$, the number of pressure holes is diluted, therefore the peaks of minimum pressure at $\phi=165^\circ$ and $\phi=195^\circ$ are not recorded. Nevertheless, the behavior is believed to remain unchanged.

At M=0.9 at $\alpha=25^\circ$ (fig. 8e), the points of minimum pressure associated with the presence of secondary vortices, move apart to $\phi=150^\circ$ and $\phi=210^\circ$, the slopes near the main vortices separation become bigger at $x/D\leq3.0$. At $x/D>3.0$ the magnitude of the maximum peaks at $\phi=135^\circ$ and $\phi=225^\circ$ remain similar, while the gradients become shallower. In addition, a slight asymmetry is noticeable at these stations. At M=1.0, the points of minimum pressure associated with the secondary vortices move further apart to $\phi=135^\circ$ and $\phi=225^\circ$ and the maximum peak at $\phi=180^\circ$ is accentuated (fig. 8f). At $x/D\leq4.0$ the pressure distribution at $75^\circ\leq\phi\leq285^\circ$ is practically constant. No asymmetry is observed at this Mach number.

3.4 Mach number and angle of attack effects

Let us look now at the angle of attack effect on the pressure distribution in the axial direction. The analysis is conducted only for the hemisphere

model, since the angle of attack effect on von-Karman model is small, and the effect on the blunted ogive model is basically similar to the effect on the hemisphere model. In fig. 10, the pressure coefficient on the leeward side as function of the axial distance from the apex (x/D), is presented at angles of attack 0°, 15°, 25°, and 45° and at M=0.5. At angles of attack less than 45°, the minimum pressure peak increases as the angle of attack is increased, but its location remains unchanged at x/D≈0.35. Further more, the angle of attack variation has practically no influence on the pressure field at stations downstream of x/D=0.5. At α=45° the location of the minimum peak moves upstream to x/D≈0.125, the pressure recovery is very quick so that at x/D≥0.7 positive pressure values are measured. At further downstream stations, an acceleration is observed. Examining the variation of the local pressure with respect to the circumferential position ϕ, at this axial station (fig. 3g), it is evident that the asymmetric flow field forces the maximum pressure peak to move away from the ϕ=180°position, thus generating the local acceleration. At M=1.0 (fig. 11), as the angle of attack increases, the zone of flow acceleration near the nose-cylinder junction becomes wider, and the location of the minimum pressure peak moves downstream. However, the magnitude of the pressure peak remains nearly constant. It is interesting to note that at α=27.5° a small acceleration is observed at x/D=2.0. In fig. 3f it is seen that at downstream stations the pressure variation tends to become more uniform, indicating the feasibility of a flow mechanism that diminishes pressure gradients by generating local flow accelerations in the vicinity of ϕ=180° and decelerating the flow at ϕ=90° and ϕ=270°.

The variation of the pressure with the axial location, from the apex downstream, at Mach numbers of 0.5, 0.9 and 1.0 is presented in fig. 12. At M=0.5 the pressure coefficient is seen to reach a minimum value at x/D=0.35 and then rapidly recover. Increasing the Mach number to 0.9 causes the minimum pressure to increase and to move to x/D=0.5. In addition, the recovery of the pressure becomes slower, until the appearance of a shock system at about x/D=1.0. Increasing the Mach number further, does not influence the location of the minimum pressure peak, but increases the value of local pressure, probably due to the detached shock upstream of the model. For the Mach 1.0 test, the pressure recovers gradually. At α=15° (fig. 13), the shock wave and the flow separation on the nose at the higher Mach number, causes a flat pressure minimum in the region 0.35<x/D<0.80 with a small maximum pressure peak at x/D=0.5, just before the minimum peak, as seen in fig. 13. The minimal pressure value obtained at M=0.5 where no shock waves and no massive separations are expected. At M=0.9 the recompression occurs on the nose area, thus increasing the pressure values there. At M=1.0 the shock appears upstream of the body, the shock system on the body is weakened and the pressure value decrease again. Beyond x/D=1.25, the pressure distribution remains independent of Mach number variations. It should be noted that the Mach effect discussed here includes also Reynolds number effect, since the Reynolds number based on the free stream velocity and the maximum diameter of the model variates from 500000 at M=0.5 to 800000 at M=1.0.

4. Discussion

The shapes of the models used in the current investigation enables the study of the effects of the nose bluntness on the pressure distribution. On the sharp and slender nosed model (e.g. the von-Karman ogive) minimum pressure peaks at ϕ=90°, 270° and a pressure recovery at ϕ=180° are measured from the first axial station at X/D=0.5, indicating that the cross flow separation starts near the apex. On the blunted nosed models (e.g. blunted ogive and hemisphere) the pressure field near the apex has a minimum peak on the leeside, and only at further downstream axial stations the crossflow separation effects on the pressure distributions are seen.

At moderate angles of attack, pressure peaks due to secondary vortices are observed on the von-Karman ogive and on the blunted ogive, however no pressure peaks due to secondary vortices in the hemisphere model case are observed, instead a plateau of approximately constant pressures is recorded.

At high angles of attack, test are conducted at several angles of roll in order to increase the resolution in the circumferential direction. The measurements at different roll angles are seen to be in good agreement on the hemisphere nosed model,thus implying that the results are roll-independent. However for the von-Karman ogive model, roll dependent results are received, specially on the nose.

One of the techniques used to validate the present data is to verify the consistency of the pressure distribution data with the integral forces and moments measurements reported in ref. 7. The measured pressures are integrated on the right hand side and on the left hand side of the model, to compute the local contribution to side force.

$$C_{y_1}(x) = \left(\frac{ds}{dx}\right)\frac{1}{\pi}\int_0^{\pi} C_p \sin\phi \frac{r(x)}{R} d\phi d\left(\frac{x}{R}\right)$$

$$C_{y_2}(x) = \left(\frac{ds}{dx}\right)\frac{1}{\pi}\int_{\pi}^{2\pi} C_p \sin\phi \frac{r(x)}{R} d\phi d\left(\frac{x}{R}\right)$$

here:

(ds/dx) - the gradient of the surface slope in the axial direction.

r(x) - local radii of the model.

R - maximum radii of the model.

The surface pressure data are interpolated using natural spline functions[11]. Each of the above integrals are evaluated by numerical integration of the spline approximated functions. The computed values are presented in fig. 14 for the case of the hemisphere-cylinder model at M=0.5 and an angle of attack of 45°.

On the model nose section, a small difference between the side forces generated on the two sides is seen indicating a small asymmetry in this zone. No asymmetry is seen at 0.5≤x/D≤1.0, but at further downstream stations a significant asymmetry is steadily building up on the cylindrical part

of the model, thus yelding a net side force similar to that observed in the integral forces data.

In order to demonstrate the usefulness of the present data, the axial pressure distribution on the hemisphere nosed model at M=0.9, 1.0 and at α=15° is compared to ref. 9. As seen in fig. 15, the presently results agree well with the data of ref. 9, although near the nose-cylinder junction a slight difference in the measured values is seen.

REFERENCES

1. Woan,C.J.; "Euler Solution of axisymmetric flows about bodies of revolution using a multigrid method" AIAA Paper 85-0017, January 1985.

2. Hartwich, P.M. and Hall, R.M.; "Navier-Stokes solution for vortical flows over a tangent-ogive cylinder", AIAA Journal Vol.28, No. 7,July 1990.

3. Zilliak, G.G.; "A computational / experimental study of the vortical flow field on a body of revolution at angle of attack". AIAA Paper 87-2277-CP, August 1987.

4. Sreekanth, A.K. and Panneerselvam, S.; "Symmetric separated flow past slender bodies at angles of attack in subsonic and supersonic flows", AIAA Paper 85-5007, October 1985.

5. Almosnino, D. and Rom, J.; "Calculation of symmetric vortex separation affecting subsonic bodies at high incidence", AIAA Journal, Vol. 21, No. 3, 1983, pp. 398-406.

6. Almosnino, D.; "High angle of attack calculations of the subsonic flow on slender bodies", AIAA Journal, Vol. 23, No. 8, 1985, pp. 1150-1156.

7. Koren, S., Arieli, R. and Rom, J.; "Measurements of lateral aerodynamic characteristics of forebodies at high angles of attack in subsonic and transonic flows", AIAA Paper no. 92-0174.

8. Bracha, J., Seginer, A. and Rom, J.; Internal Report, Aerodynamic Laboratories, Technion, TAE Report No. 0-143, May 1975.

9. Hsieh, T.; "An investigation of separated flow about a hemisphere-cylinder at 0 to 19 deg incidence in the Mach number range from 0.6 to 1.5". AEDC-TR-76-112, November 1976.

10. Degani, D and Schiff, L.B.; "Numerical simolation of the effect of special disturbances on vortex asymmetry". AIAA Paper 89-0340, January 1989.

11. Ahlberg, J.H., Nilson, E.N. and Walsh, J.L.; "The theory of splines and their applications", Mathematics in Science and Engineering, Vol. 38, Academic Press, 1967.

12. Lamont, P.J. and Hunt, B.L.; "Pressure and force distributions on a sharp-nosed circular sylinder at large angles of inclinatio to a uniform subsonic stream". J. Fluid Mechanics, 1976, vol. 76, part 3, pp.519-559.

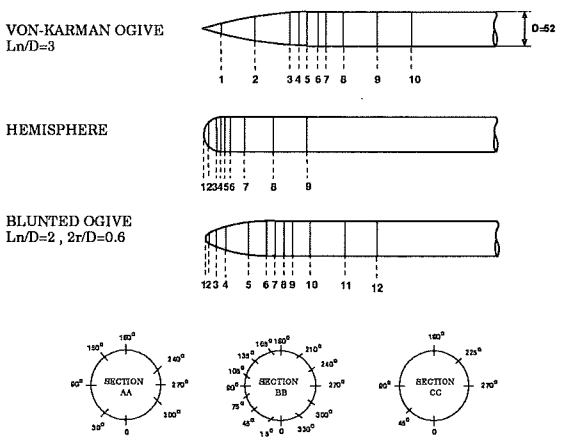

X Station	Von-Karman		Hemisphere		Blunted ogive	
	x/D	Section	x/D	Section	x/D	Section
1	0.5	AA	0	-	0	-
2	1.5	AA	0.125	AA	0.1	AA
3	2.5	BB	0.35	BB	0.3	AA
4	2.75	BB	0.5	BB	0.6	AA
5	3.0	BB	0.65	BB	1.25	BB
6	3.25	BB	0.8	BB	1.75	BB
7	3.5	BB	1.25	CC	2.0	BB
8	4.0	CC	2.0	CC	2.25	BB
9	5.0	CC	3.0	CC	2.5	BB
10	6.0	CC			3.0	CC
11	-				4.0	CC
12	-				5.0	CC

Fig. 1 - Sketch of the geometry of the models and the pressure holes location.

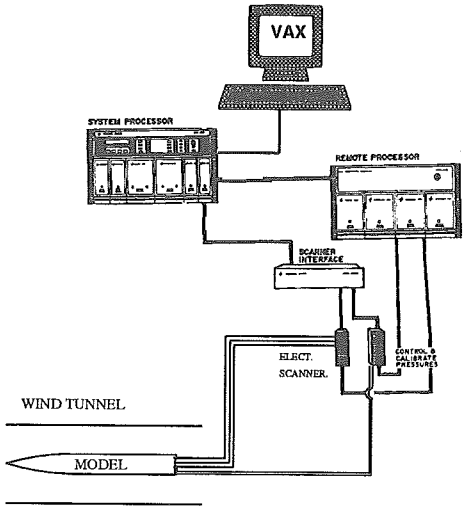

Fig. 2 - Sketch of the measurement system configuration.

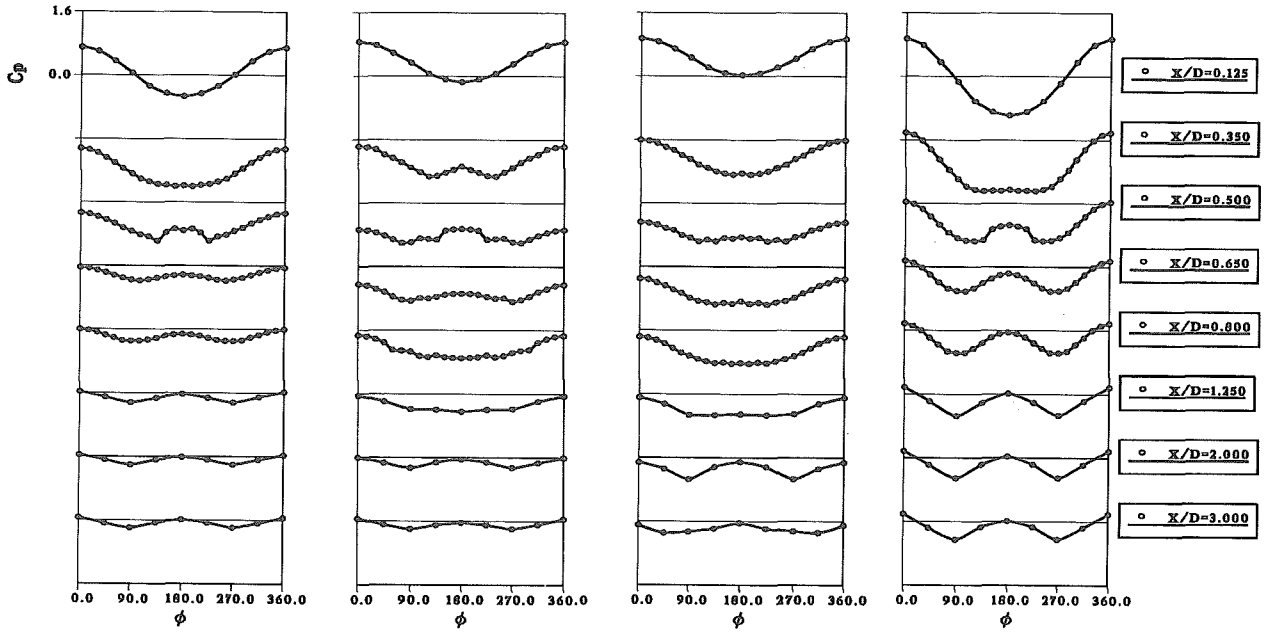

a) M=0.5, α=15° b) M=0.9, α=15° c) M=1.0, α=15° d) M=0.5, α=25°

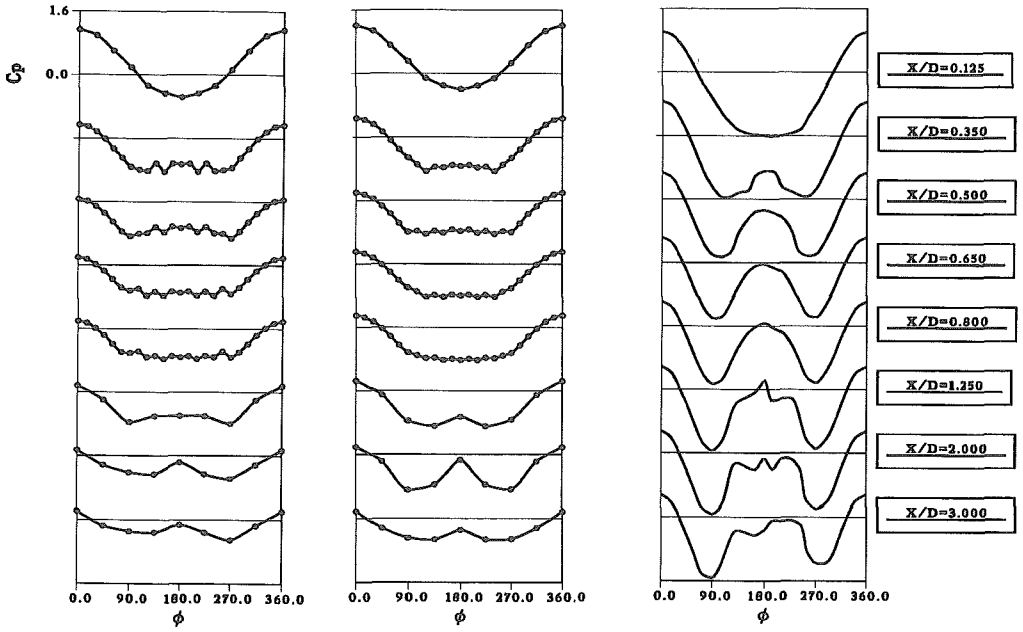

e) M=0.9, α=27° f) M=1.0, α=27.5° g) M=0.5, α=45°

fig. 3 - Variation of the pressure coefficient as function of the circumferencial angle and the axial station, on the hemisphere nosed model.

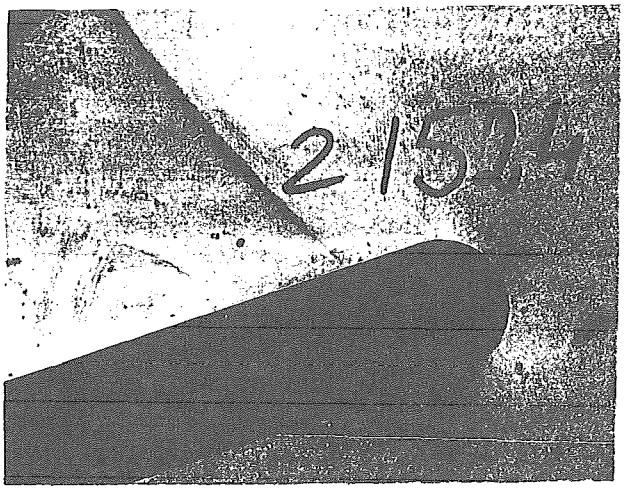

Fig. 4 - Shlieren visualization of the hemisphere model at M=1.0 and α=15°.

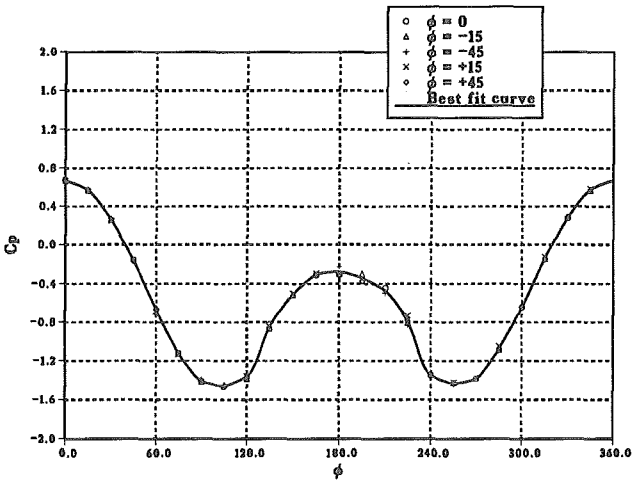

Fig. 5 - Pressure measurements on the hemisphere model at several roll angles. x/D=1.0, M=0.5, α=45°.

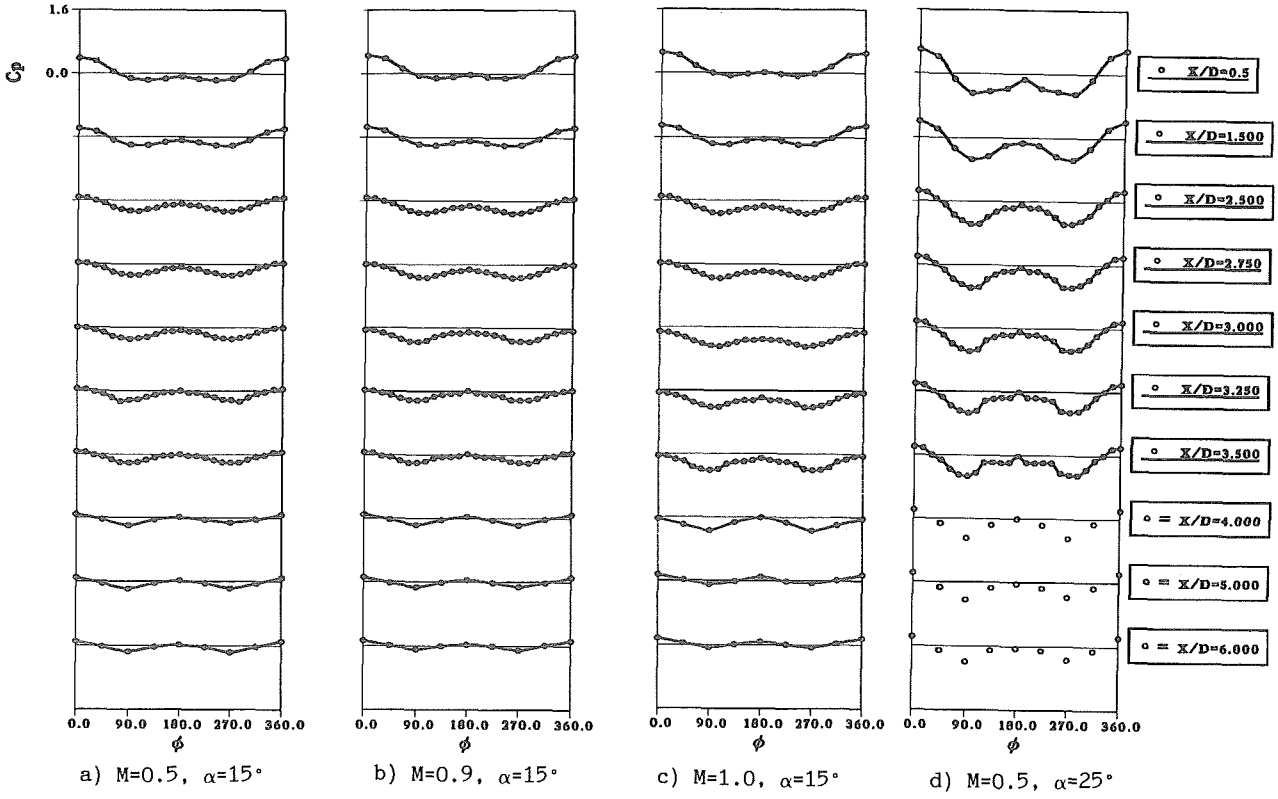

a) M=0.5, α=15° b) M=0.9, α=15° c) M=1.0, α=15° d) M=0.5, α=25°

fig. 6 - Variation of the pressure coefficient as function of the circumferencial angle and the axial station, on the von-Karman ogive model.

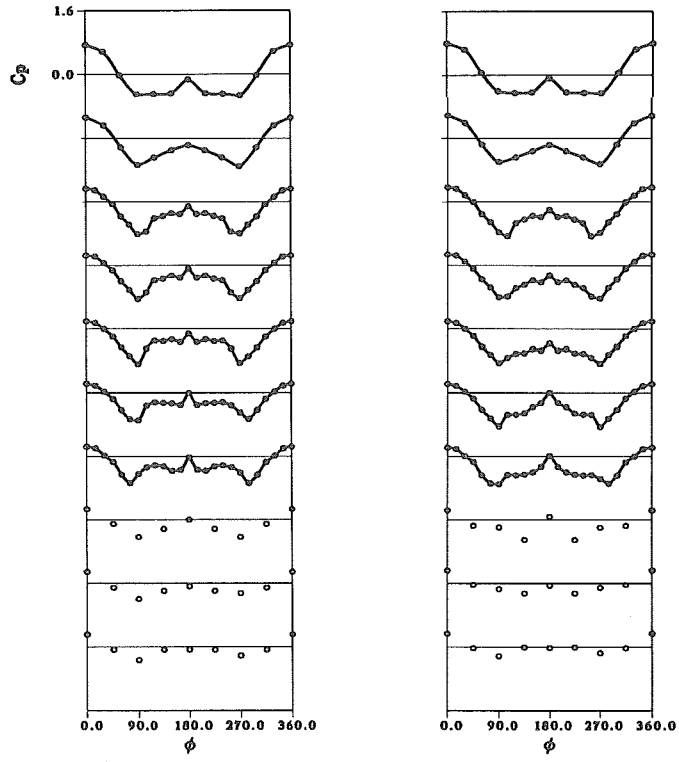

e) M=0.9, α=27°

f) M=1.0, α=27.5°

g) M=0.5, α=45°

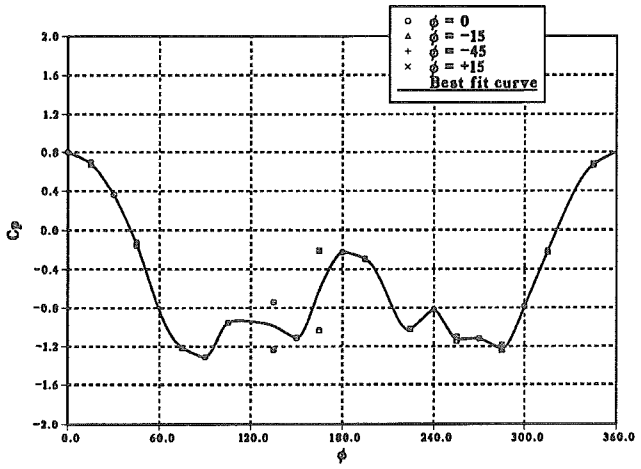

Fig. 7 a) - Pressure measurements on the von-Karman model at several roll angles. x/D=1.5, M=0.5, α=45°.

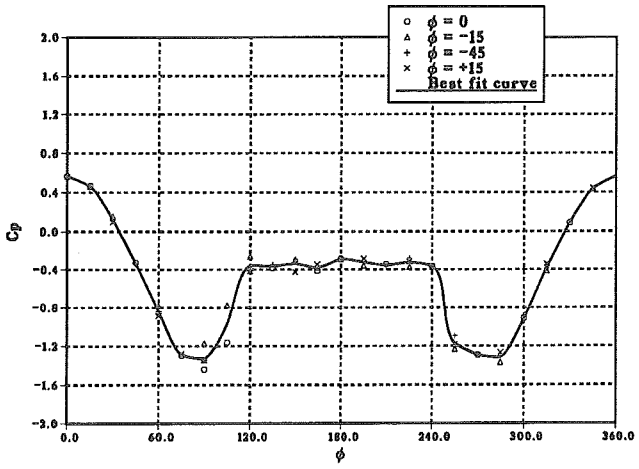

Fig. 7 b) - Pressure measurements on the von-Karman model at several roll angles. x/D=3.0, M=0.5, α=45°.

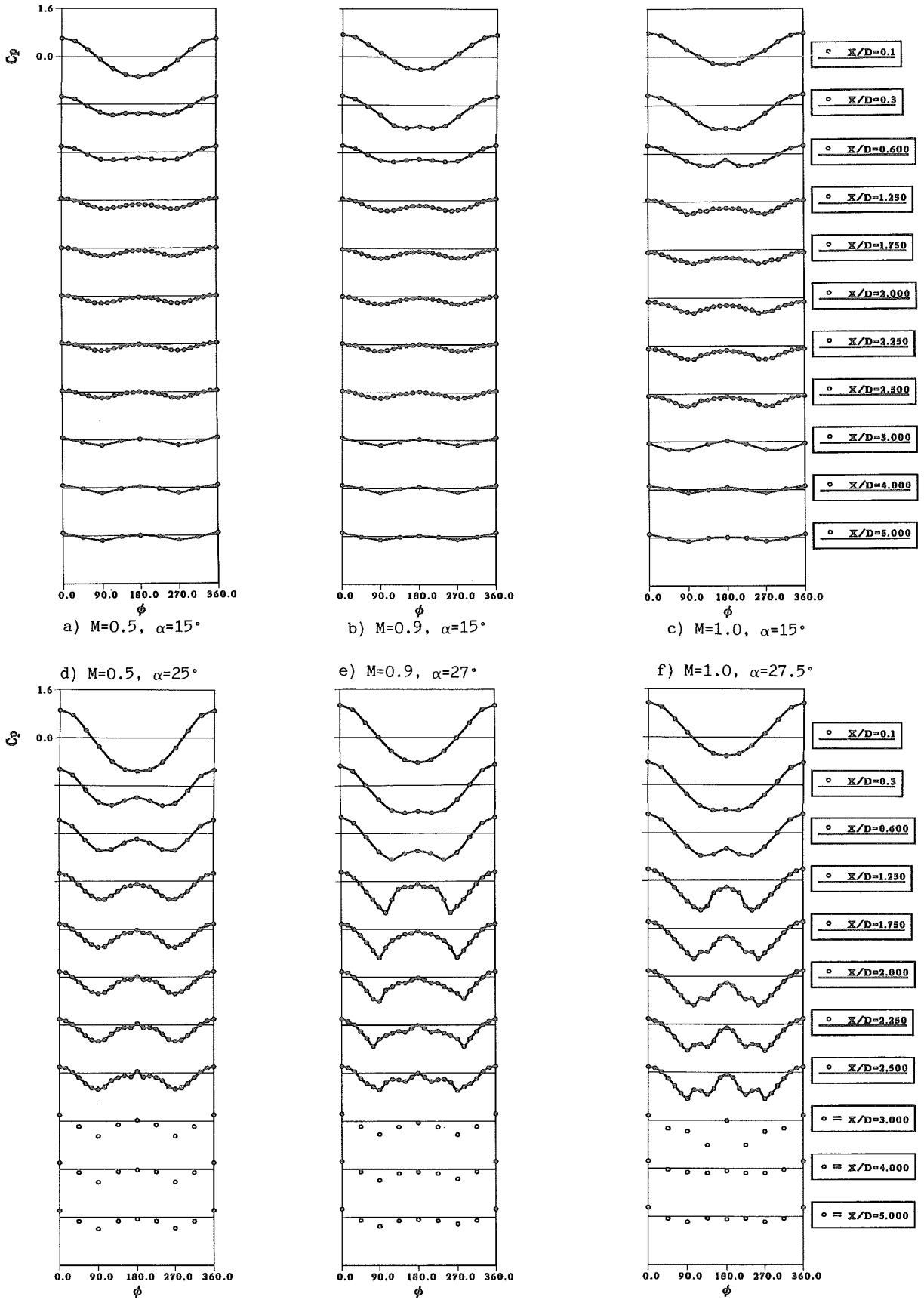

fig. 8 - Variation of the pressure coefficient as function of the circumferencial angle and the axial station, on the blunted ogive model.

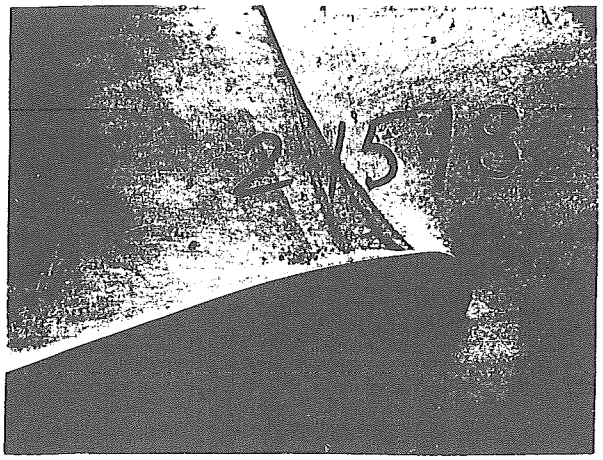

Fig. 9 - Shlieren visualization of the blunted ogive model at M=1.0 and α=15°.

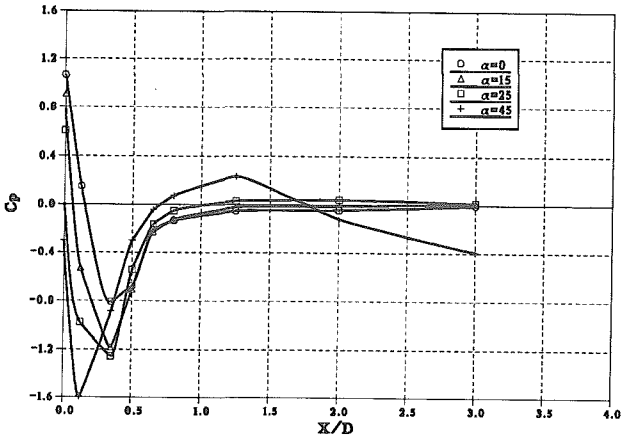

Fig. 10 - Pressure distribution on the leeward side as function of x/D, on the hemisphere model, at several angles of attack and M=0.5.

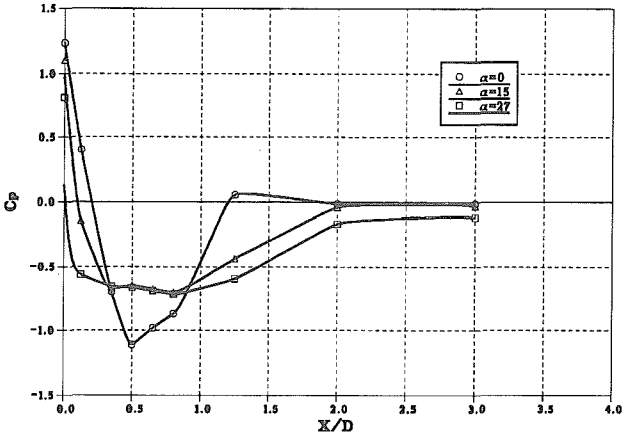

Fig. 11 - Pressure distribution on the leeward side as function of x/D, on the hemisphere model, at several angles of attack and M=0.9.

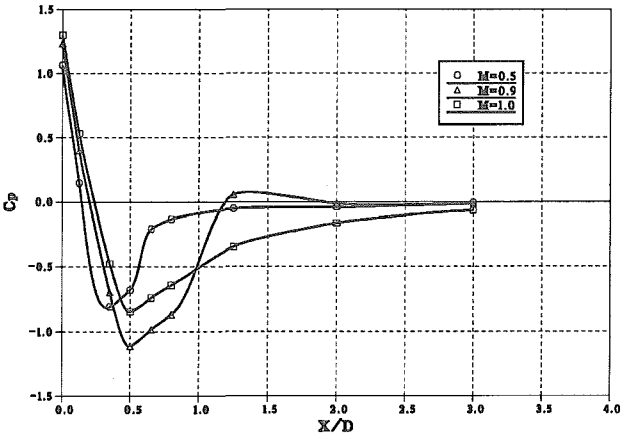

Fig. 12 - Pressure distribution on the leeward side as function of x/D, on the hemisphere model, at several Mach numbers and α=0°.

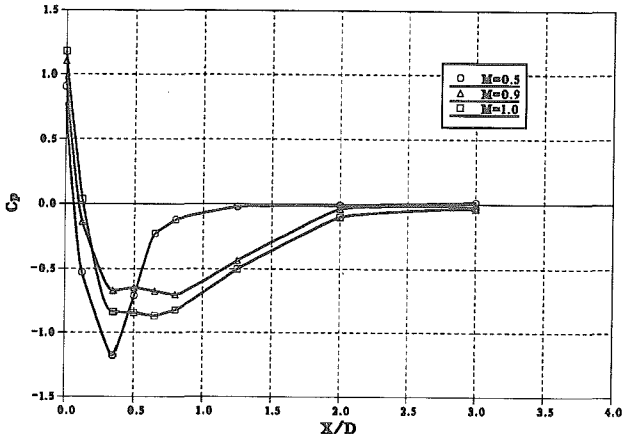

Fig. 13 - Pressure distribution on the leeward side as function of x/D, on the hemisphere model, at several Mach numbers and α=15°.

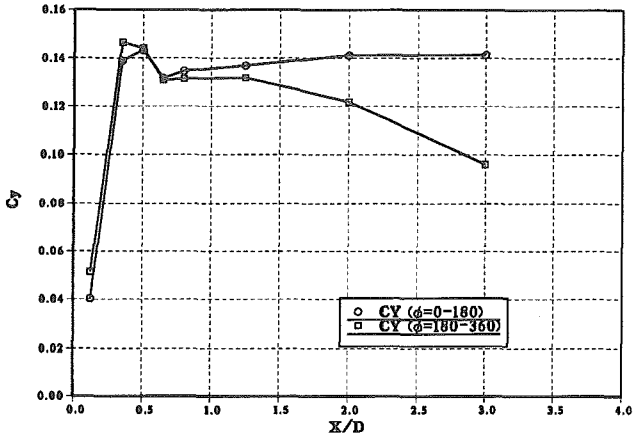

Fig. 14 - Side force variation on the hemisphere model as function of X/D. M=0.5, α=45°.

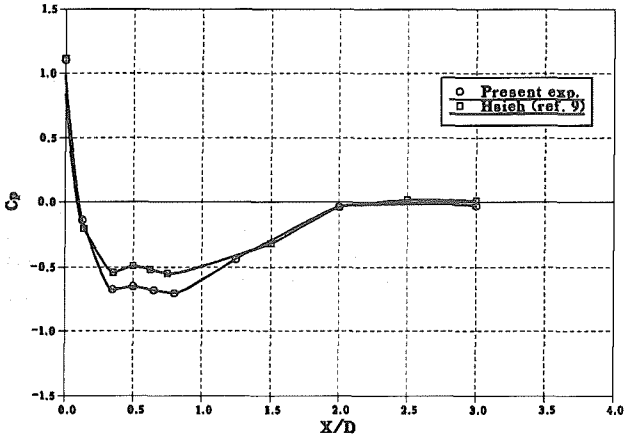

Fig. 15 - Comparison with data from ref. 9. Hemisphere cylinder model, M=0.9, α=15°.